https://doi.org/10.5194/wes-2026-155
Preprint. Discussion started: 9 September 2026

eawe european academy of wind energy
Open Access WIND ENERGY SCIENCE DISCUSSIONS

Influence of inflow turbulence intensity on static and dynamic stall of NACA 0021 at Re$= 5.5 \times 10^6$ using DDES method

Hye Rim Kim[1] and Lars Wein[1]

[1]Institute of Turbomachinery and Fluid Dynamics, Leibniz University Hannover, Germany

Correspondence: Hye Rim Kim (kim@tfd.uni-hannover.de)

Abstract. Airfoil aerodynamics at high Reynolds numbers (on the order of 10^6) are of significant interest due to the increasing dimensions of wind turbine rotors. Recent studies indicate that the stall mechanisms at high Reynolds numbers differ from those at lower values, raising questions regarding the validity of conventional low-order prediction tools for simulating aerodynamic performance under these conditions. In this study, static and dynamic stall simulations employing Unsteady Reynolds-Averaged Navier–Stokes (URANS) and Delayed Detached Eddy Simulation (DDES) methods are validated against experimental data for a NACA 0021 airfoil at Re=5.5×10^6. Firstly, two spanwise extensions of a Q3D model are simulated using URANS. Results demonstrate that an aspect ratio (AR) of 0.25 is insufficient for accurately capturing large-scale stall cells, resulting in overpredicted lift values. Subsequent simulations with AR$= 2.5$ confirm that the assumption of fully turbulent boundary layers is valid at such high Reynolds numbers. The DDES method—a hybrid approach combining RANS and LES—shows promise in predicting both the abrupt onset of stall and turbulent flow separation with minimal additional computational cost. Further simulations using DDES with varying inflow turbulence intensities reveal a stall-delay effect as freestream turbulence increases. While the sensitivity of freestream turbulence on dynamic stall during airfoil pitching is negligible, it significantly influences post-stall behaviour. Spectral analysis indicates that the post-stall regime is dominated by the shedding of dynamic stall vortices at a Strouhal number of 0.5.

1 Introduction

The currently built wind turbines in the offshore wind farms are ranging from 10 to 15 MW, reaching the airfoil chord-based Reynolds numbers between $3...15 \times 10^6$ (Gaertner et al., 2020). With ongoing developments aiming for rated powers up to 22 MW, future turbines are expected to operate at the Reynolds numbers $8...18 \times 10^6$ (Zahle et al., 2024). The aerodynamic performance of wind turbines is conventionally predicted using low-order models, such as the vortex panel or vortex lattice methods. These models are featured with additional corrections to account for viscous effects, particularly for predicting near-stall and post-stall behaviour. Dynamic stall predictions further require additional analytical models with empirical coefficients, such as the Beddoes-Leishman model (Leishman and Beddoes, 1989; Hansen et al., 2004). While these models have been validated and recalibrated against experimental data at low Reynolds numbers, their validity at higher Reynolds numbers remains uncertain. This is primarily due to the challenges associated with conducting scaled experiments under high Reynolds number, incompressible conditions (low Mach numbers), which require specialised wind tunnels capable of high pressure and

https://doi.org/10.5194/wes-2026-155
Preprint. Discussion started: 9 September 2026

eawe european academy of wind energy
Open Access WIND ENERGY SCIENCE DISCUSSIONS

flow rates. Although high-fidelity numerical methods, such as Large-Eddy Simulation (LES) and Direct Numerical Simulation (DNS), offer alternatives to experimental validation, their computational costs are extremely high at multi-million Reynolds numbers. As a compromise, hybrid RANS-LES approaches, such as Detached Eddy Simulation (DES), are alternatives for simulating flow at high Reynolds numbers (Athkuri et al., 2026).

1.1 Stall characteristics at high Reynolds numbers

Despite the challenges, recent studies have investigated dynamic stall at multi-million Reynolds numbers. At low Reynolds numbers, stall is typically initiated by the bursting of the laminar separation bubble (LSB) near the leading edge (leading-edge stall). The detailed flow feature at the onset of this laminar stall for NACA 0012 at Re$= 0.2 \times 10^6$ is investigated by Visbal and Benton (2018) using LES. However, experimental investigations at higher Reynolds numbers reveal a change in the stall onset mechanism (Brunner et al., 2021a; Kiefer et al., 2022), where they conducted static and dynamic stall experiments on NACA 0021 airfoil at a wide Reynolds numbers range (Re$= 0.5...7.9 \times 10^6$). According to the studies, the laminar to turbulent transition occurs close to the leading-edge above Re$= 2.5 \times 10^6$, preceding the position of LSB typically observed at low Reynolds numbers. Therefore, at these high Reynolds numbers, the stall onset is characterised by turbulent separation instead of laminar separation. The turbulent boundary layer near the leading edge enhances flow attachment, resulting in a high lift peak prior to stall, followed by an abrupt decrease in lift once stall onset. Similar trends were observed in experiments by Chellini et al. (2024, 2026) on the FFA-W3-211 airfoil at Re$= 0.5...3.5 \times 10^6$. This abrupt stall onset associated with turbulent separation can be further found in Ladson (1988) (NACA 0012 at Re$= 2...12 \times 10^6$), and Ceyhan et al. (2017) (DU00-W-212 at Re$= 15 \times 10^6$). In constrast to these findings, the early study by Jacobs (1931) shows no signature of abrupt stall onset at Re$= 3.2 \times 10^6$ for the NACA 0021 airfoil, rather a gradual decrease in lift coefficients. This discrepancy may be attributed to differences in test setup, e.g. measurement method (total blade force using balance beams) and high freestream turbulence in the wind tunnel. Numerical investigations by the authors (Kim et al., 2025a, b) on the FFA-W3-211 airfoil at Re$=15 \times 10^6$ support the experimental observations: transition to turbulent boundary layer occurs near the leading-edge, which delays the onset of both static and dynamic stall due to enhanced flow attachment. The maximum lift coefficients reaches $C_l = 2$ before the onset of static stall, and it further increases during dynamic pitching.

1.2 Three-dimensional stall cells

The stalled flow over an airfoil is characterised by the three-dimensional stall cells (Fig. 1). These structures typically exhibit a wavelength of one to two times the chord length, although this depends on the specific airfoil geometry. Capturing these large-scale flow features is both experimentally and numerically demanding; as a result, investigations often employ small finite-span airfoils.

Experimental setups inherently constrain the aspect ratio (AR) of the finite airfoil sections for wind tunnel tests, which has a significant influence on stall cell formation. The use of either open-end or wall-closed configurations introduces tip-vortices or viscous wall-effect. To eliminate these effects, wind tunnel corrections are widely applied (Jacobs, 1931). While these correction methods are well validated for attached flow regimes, their validity and accuracy in stalled flow region, where

https://doi.org/10.5194/wes-2026-155
Preprint. Discussion started: 9 September 2026

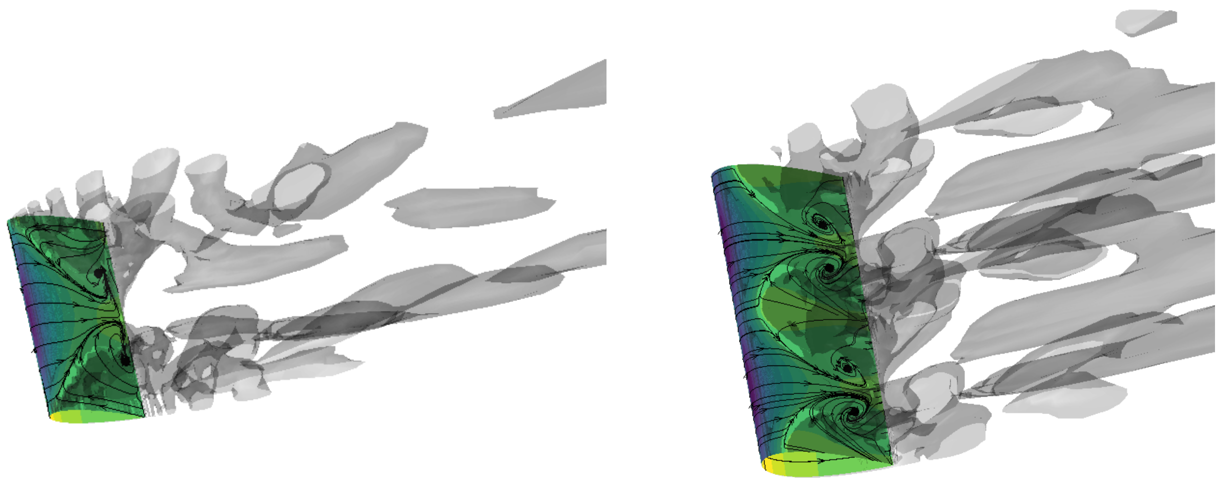

Figure 1. Different stall cell formation with aspect ratio (AR) of 2.5 and slip-walls as boundary conditions (left), and AR$= 2.5$ and periodic boundary conditions, with the assumption of infinite span, visualised in AR$= 5$ (right)

strong three-dimensional stall cells exist, remain uncertain. The impact of AR on the number and size of stall cells has been studied experimentally by Winkelman and Barlow (1980). At a low Reynolds number of Re$= 0.385 \times 10^6$, they observed a single-centered stall cell for AR$= 3$, and multiple stall cells for AR> 6. Similarly, Yon and Katz (1998) show that the criterion for a single stall cell to form is AR~ 1.5. Both Winkelman and Barlow (1980) and Yon and Katz (1998) show that the number of stall cells increasing approximately linearly with AR. Analytical work by Gross et al. (2015) further demonstrated that the spanwise extension of stall cells per chord is a function of the lift curve slope in the stall region. Extensive measurements using oil-visualisation and PIV by Ragni and Ferreira (2016) on a finite airfoil of AR$= 4.8$ at Re$= 1 \times 10^6$ revealed large variation of sectional lift coefficient along the span; particularly, a large separation region found at the midspan, corresponding to low sectional lift, while the other spanwise positions exhibited higher lift. This is an indication of a centered stall cell in the span. The studies addressed above with high AR concern low Reydnols numbers. Experimental setups at high Reynolds numbers feature AR< 2 and the aerodynamic forces are only measured at midspan. Therefore, these data likely represent only the center of a stall cell in case of open-end configuration, or the extreme outside of stall cells for airfoils with end walls (see Fig. 1 left), rather than the spanwise-averaged performance relevant for full-scale rotor in reality.

Numerically, small AR models or even AR=0 (2D domain) with a translational periodicity in the span are commonly used to reduce computational expense. AR$= 0.2$ is often used for LES simulations (Montalà et al., 2026). However, such restricted span extension is not able to resolve the large-scale three-dimensional stall cells accurately. The abrupt stall onset observed experimentally at high Reynolds numbers cannot be reproduced with 2D-domains (Ceyhan et al., 2017; Athkuri et al., 2026). Athkuri et al. (2026) reported that their previous 2D simulations failed to correctly predict the stall onset angle and the abrupt

https://doi.org/10.5194/wes-2026-155
Preprint. Discussion started: 9 September 2026

onset characteristic at Re$= 6 \times 10^6$; however, 3D hybrid RANS-LES simulations using the one equation Spalart-Allmaras turbulence model (SA) achieved good agreement with experimental data in terms of the abrupt decrease in lift. The influence of AR has also been addressed at lower Reynolds numbers. For instance, using LES and DNS, Montalà et al. (2026) investigated the SD7003 airfoil at Re$= 0.06 \times 10^6$, finding that AR> 0.8 is sufficient for the accurate prediction of flow separation and wake. They showed that the insufficient AR induces artificial turbulent structures near the trailing edge, leading to overpredictions of lift, drag, and their fluctuations in stalled conditions. Similarly, using DES and LES methods, Haase et al. (2010) and Park et al. (2017) examined deep stall (angle of attack of 60°) characteristics of NACA 0021 airfoil at Re$= 0.27 \times 10^6$, and found that both integral quantities and spectral contents converge for AR> 2; for AR< 2, artificially lower suction-side pressure resulted in increased lift coefficients.

1.3 Influence of freestream turbulence intensity

Wind turbines are operated within the atmospheric boundary layer, where the freestream velocity profile and associated turbulence characteristics exhibit significant temporal fluctuation (Kosović et al., 2026). For offshore megastructures, the rotor blades traverse a wide range of altitudes during a single rotation, encountering different flow regimes-from the turbulent Prandtl layer near the surface to the laminar Ekman layer at high altitude of 500-1000 m (Neuhaus et al., 2024). Additionally, turbines within wind farms are subject to increased turbulence intensity due to the wakes of upstream ones. Therefore, sensitivity studies of various inflow conditions on aerodynamic performance and stall characteristics are necessary. At low Reynolds numbers on the order of $\sim 10^5$, both numerical and experimental studies have been conducted to examine the influence of freestream turbulence (Huang et al., 2020; Damiola et al., 2023). The LES-based study from Huang et al. (2020) with the synthetic turbulent inflow showed that the freestream turbulence has a significant impact on the onset of static stall: increasing turbulence intensity led to a delayed stall onset as the boundary layer is stabilised near separation. During periodic pitching of the airfoil, the freestream turbulence intensity had minimal impact during the up-pitching phase, but a significant impact during down-pitching, enhancing the flow reattachment. Despite these insights at low Reynolds numbers, the investigations on the impact of freestream turbulence on static and dynamic stall at high Reynolds number conditions remain limited in the literature.

1.4 Objectives

This study addresses the necessity of high aspect ratio 3D-simulations to accurately capture stall phenomena on both static and pitching airfoils. Using the computationally affordable DDES method, the static and dynamic stall behaviour of NACA 0021 is investigated, with a particular focus on the effect of freestream turbulence intensity. The detailed objectives of the current work are as follows:

- Verification of static and dynamic stall simulations at a high Reynolds number (Re$= 5.5 \times 10^6$), utilising experimental data from Brunner et al. (2021a) and Kiefer et al. (2022)
- Assessment of the influence of aspect ratio on the static stall prediction
- Comparison of DDES method against the URANS method for stall predictions

https://doi.org/10.5194/wes-2026-155
Preprint. Discussion started: 9 September 2026

– Investigation on the influence of inflow turbulence intensity on static and dynamic stall at high Reynolds number

2 Methodology

2.1 Experimental data from Brunner et al. (2021a, b) and Kiefer et al. (2022) and wind tunnel correction

Brunner et al. (2021a) and Kiefer et al. (2022) published the experimental data for the NACA 0021 airfoil under static and ramp-up type dynamic motion conditions. The closed-loop and pressurised wind tunnel provides a low Mach number on the order of 0.01, while simultaneously achieving a high chord-based Reynolds number up to $\mathrm{Re}_\infty = 5.5 \times 10^6$. The finite-span airfoil had a chord length of $c = 0.17$, and aspect ratio (AR) of 1.5, equipped with end-plates. The freestream velocity is $U_\infty = 3.31$ m/s for this Reynolds number.

Experimental data obtained with finite-span airfoils in wind tunnels require specific corrections. According to Brunner et al. (2021a), an 8.7% velocity correction was applied to account for blockage effects due to the airfoil and support structures, which affects the normalisation of the lift coefficient C_l and drag coefficient C_d. Additionally, the corrections on the angle of the attack α and C_d are applied to account for tip vortex and downwash effects. The angle of attack α is corrected only up to $\alpha < 26°$ in the attached flow region; for the stalled region, the angle is simply shifted to create continuos curves, as described in Brunner et al. (2021a). The example is shown in Fig. 2, indicating that the stall onset angle in the uncorrected data is 26°, while it is 17.5° in the corrected data. Throughout the paper, the corrected data is represented and compared with simulation results unless otherwise mentioned.

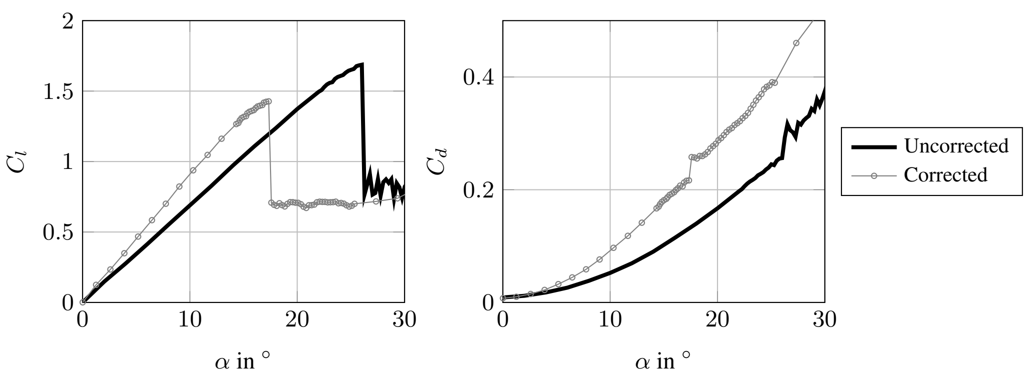

Figure 2. Uncorrected and corrected experimental data of of NACA 0021 at Re$= 5.0 \times 10^6$ from Brunner et al. (2021b)

The dynamic stall data from Kiefer et al. (2022) are not corrected in the original dataset. To compare them with simulation results, the experimental data are corrected by the authors using the same scaling technique described in Brunner et al. (2021a) for the static dataset. However, it should be noted that the correction method applied in the stalled flow region, especially in dynamic conditions, have not been validated in literatures. Therefore, the comparison of both static and dynamic stall flow should be interpreted with caution.

https://doi.org/10.5194/wes-2026-155
Preprint. Discussion started: 9 September 2026

2.2 Numerical method and test cases

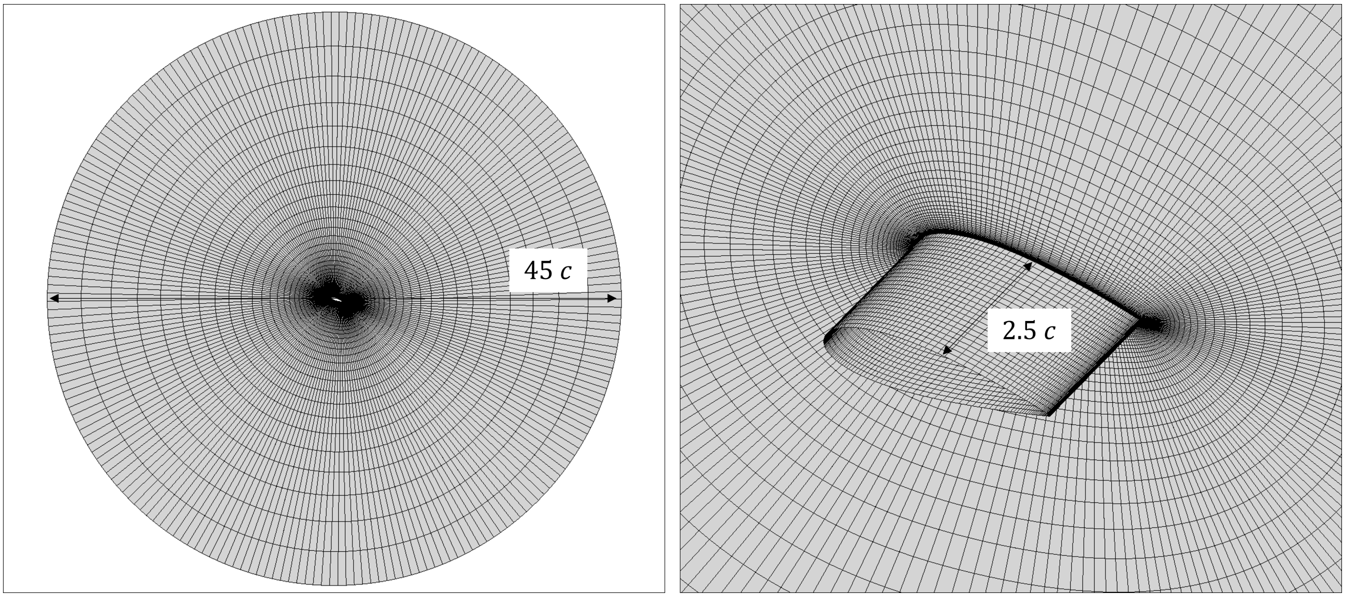

Figure 3. Simulation domain and mesh: 2D-view of the computational domain, including the farfield boundaries (left), and zoomed-in 3D view, showing the surface meshes on the airfoil and the periodic wall on one side (right)

The NACA 0021 airfoil with a chord length of $c = 0.17$ m is modelled for the numerical simulations, identical to the experimental configuration from Brunner et al. (2021a); Kiefer et al. (2022). The outer domain representing farfiled has a diameter of $45\ c$. Two different spanwise extensions of $0.25\ c$ and $2.5\ c$ are modelled. The spatial discretisation in the vicinity of the airfoil achieves y^+ smaller than 1, and the outer region is coarsely meshed with the assumption of freestream. In chordwise direction, the leading-edge and trailing-edge regions are finely meshed, while the mid-chord region is coarser, resulting in a maximum x^+ of 800. For both aspect ratios (2.5, and 0.25), the spanwise length is discretised into 25 cells, which corresponds to z^+ of 2000 and 200, respectively. The same mesh is used for both URANS and DDES simulations, which has the total number of cells of 0.46×10^6, after conducting grid convergence studies (see Appendix A).

The transient, incompressible pimpleFoam solver from OpenFOAM v2412 is used to validate the low Mach number condition. For temporal discretisation, a second-order implicit backward differencing scheme was selected (ddtSchemes), providing both stability and accuracy for unsteady calculations. To approximate spatial gradients, a cell-limited Gauss linear scheme (cellLimited Gauss linear 1.0) was utilised for all variables, to prevent non-physical oscillations while maintaining second-order accuracy. Convective terms were discretised using the Gauss linearUpwind scheme for velocity, with limited-linear schemes for turbulence quantities to further control numerical diffusion and boundedness. Diffusive terms were treated with a Gauss linear limited corrected scheme, incorporating a non-orthogonality correction factor of 0.5 to enhance accuracy on non-orthogonal

https://doi.org/10.5194/wes-2026-155
Preprint. Discussion started: 9 September 2026

meshes. Interpolation across cell faces employed linear interpolation, and surface-normal gradients were limited and corrected in line with the diffusive discretisation.

A fixed viscosity with Newtonian transport model is used. For the Unsteady Reynolds-Averaged Navier–Stokes (URANS) simulations, two turbulence models are employed for comparative purposes. The first is the two-equation $k-\omega$ Shear Stress Transport (SST) model, referred to as kOmegaSST, originally developed by Menter (1994). The kOmegaSST model combines the robust near-wall performance of the $k-\omega$ formulation with the free-stream independence of the $k-\epsilon$ model, enabling reliable prediction of boundary layer separation under adverse pressure gradients. Additionally, the four-equation Langtry–Menter $k-\omega$ SST model with the $\gamma-\mathrm{Re}_\theta$ transition model (implemented in OpenFOAM as kOmegaSSTLM) is utilised to account for transitional flow effects (Langtry and Menter, 2009). This model introduces transport equations for the intermittency (γ) and transition Reynolds number (Re_θ), providing a framework to predict laminar-to-turbulent transition in boundary layers. The combination of these two turbulence models allows for verification of the fully turbulent assumption at the high Reynolds numbers investigated in this study. By comparing results from the standard kOmegaSST model, which assumes fully turbulent flow, to those from the kOmegaSSTLM model, which can capture transitional behaviour, the suitability of the fully turbulent modeling approach at the selected flow conditions is assessed.

For the Delayed Detached-Eddy Simulation (DDES), the turbulence model kOmegaSSTDDES is employed within OpenFOAM. This model builds upon the baseline $k-\omega$ SST framework, and incorporates the DDES formulation to provide a seamless transition between RANS and LES regimes. The grid filter width for the sub-grid scale (SGS) modeling is set using the *delta*, with the specific method tailored to the grid characteristics of the computational domain. To limit the maximum grid filter width and ensure appropriate length scales for resolving turbulent structures, the parameter maxDeltaxyzCoeffs is set to 2, following best practices for hybrid RANS-LES approaches in OpenFOAM. These settings help achieve a balance between accuracy in the LES region and computational efficiency, while minimizing modelled stress depletion and grid-induced separation in the RANS regions.

The outer surface of the farfield domain uses the freestreamVelocity boundary conditions, which automatically switches between a fixed freestream velocity at inflow ($U_\infty = 3.31$ m/s) and a zero-gradient at outflow boundaries. Side walls are set with cyclicAMI with translational periodicity, so the domain itself has a finite span length, but the infinite airfoil is assumed. The airfoil surface is set to a non-slip wall (noSlip) for static cases, and a movingWallVelocity for dynamic cases, allowing for changing angle of attack during simulation. The maximum CFL number is set to 10, resulting in a time-step size on the order of 1e-4 s. Static simulations are conducted for 20 s, which is significantly longer than the through-flow time across the entire domain (2.3 s), to achieve convergence of large-scale stall cells.

The simulation cases are summarised in Tab. 1. Static cases are focused on the nonlinear region between angle of attack 10...29°, covering the stall onset and deep-stall regions. The pitching-up condition from Kiefer et al. (2022) is uncorrected angle of attack between 19°...29°, following a quater-period of sinusoidal curve. This corresponds to the airfoil pitching between either 12.17...20.31° (Pitching A) or 12.17...25.17° (Pitching B), depending on whether the angle of attack in the stalled region is corrected or not. The turbulence intensity prescribed at the inlet of the farfield domain is not representative

https://doi.org/10.5194/wes-2026-155
Preprint. Discussion started: 9 September 2026

Table 1. Overview of simulation cases

Case	AR	Turbulence modelling	TI in %	Static/Dynamic
1	2.5	RANS SST + $\gamma - \mathrm{Re}_\theta$	2.0	S, D
2	2.5	RANS SST	2.0	S
3	0.25	RANS SST + $\gamma - \mathrm{Re}_\theta$	2.0	S
4	2.5	RANS SST + $\gamma - \mathrm{Re}_\theta$	4.8	S, D
5	2.5	RANS SST	4.8	S
6	0.25	RANS SST + $\gamma - \mathrm{Re}_\theta$	4.8	S
7	2.5	DDES SST	2.0	S, D
8	2.5	DDES SST	4.8	S, D
9	2.5	DDES SST	0.5	S, D
10	2.5	DDES SST	3.6	S, D
11	2.5	DDES SST	9.6	S, D

of that experienced by the airfoil, as it decays rapidly from the domain inlet to the airfoil. Therefore, the listed turbulence intensities are probed from the flow solution near the leading-edge as the apparent TI for the airfoil.

The integral values such as the lift coefficient C_l and the drag coefficients C_d are area-averaged over the entire span of the airfoil, unless otherwise speficied. They are averaged over the last 10 seconds of the solutions, after achieving the convergence. The spanwise variation of these coefficients, due to the large-scale stall cells, is indicated as shaded regions in the figures. In order to further characterise stall cell behaviour and the decay process during dynamic stall events, additional frequency analysis is performed, capturing the spectral contents of stall vortices.

2.3 XFOIL

XFOIL uses a vortex panel method with the capacity of calculating boundary layers for viscous flows at different Reynolds and Mach numbers. The code efficiently computes the aerodynamic lift and drag of 2D airfoils in subsonic conditions. Transition from laminar to turbulent boundary layers is either calculated by the solver or forced at the leading edge, with the assumption of the fully turbulent boundary layers at high Reynolds numbers.

3 Influence of Numerical Setup

3.1 2D-XFOIL prediction

Figure 4 shows the corrected measurement data from Jacobs (1931) at Re$= 3.2 \times 10^6$ as well as from Brunner et al. (2021b) at Re$= 3.0 \times 10^6$ and Re$= 5.0 \times 10^6$, compared with the XFOIL calculations for different transition parameters. Comparing the two measurement data sets, the corrected C_l agrees well in the attached flow regime, while significant deviation is observed in C_d, particularly in the attached region. As the order of magnitude of C_d from Brunner et al. (2021b) is higher compared

https://doi.org/10.5194/wes-2026-155
Preprint. Discussion started: 9 September 2026

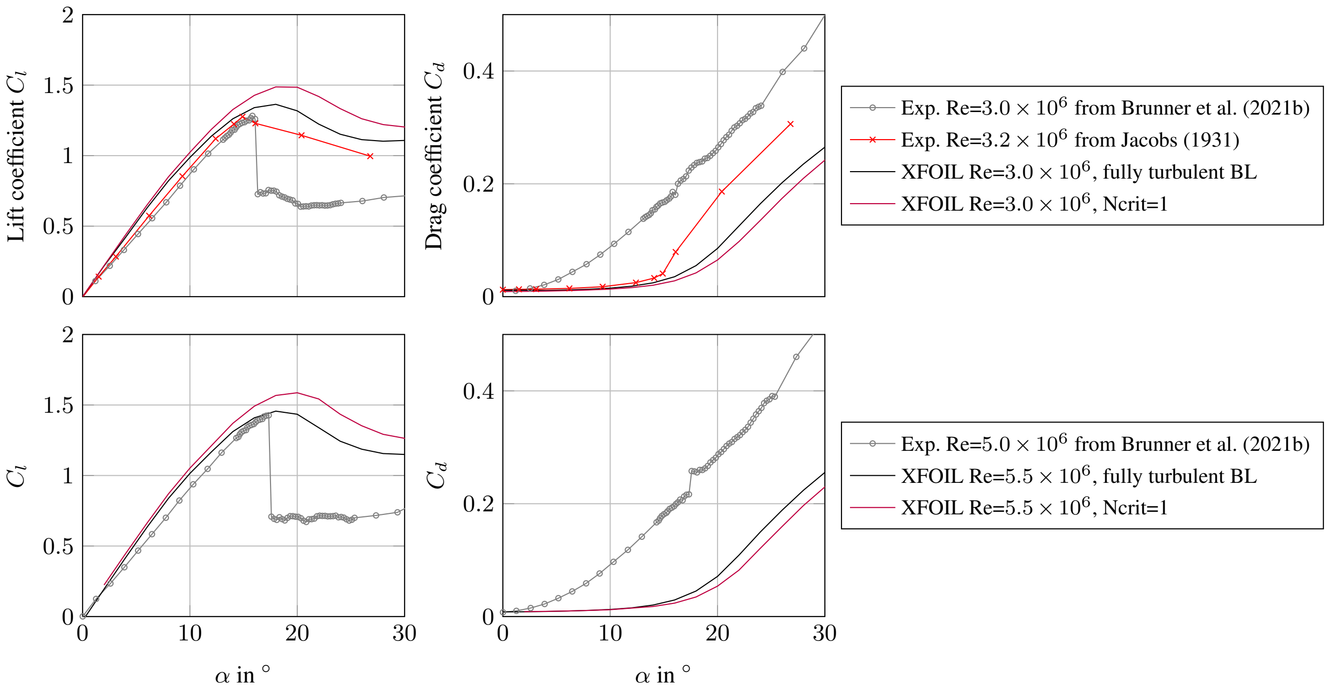

Figure 4. Static polars of NACA 0021 at Re$= 3.0 \times 10^6$, 5.0×10^6, and 5.5×10^6 from Jacobs (1931); Brunner et al. (2021b) and XFOIL predictions with different transition model settings

Table 2. Comparison between experiments from Jacobs (1931) and Brunner et al. (2021a)

	Brunner et al. (2021a)	Jacobs (1931)
Inflow turbulence	Low (0.3 ... 1.1 %)	High
Aspect ratio	1.5 with end-plates	6 (open-end)
Measurement of force	Pressure taps at the midspan	Total force using balance beams
Wind tunnel correction	Only attached flow region	All angle of attack

to the data from other literatures, the XFOIL result is well validated against Jacobs (1931) in this region. After the stall onset near $\alpha_{ss} = 17°$, Brunner et al. (2021a) observe an abrupt decrease in C_l, while Jacobs (1931) shows a more gradual decrease (trailing-edge stall). The large deviation in the stall region has been attributed primarily to the difference in freestream turbulence intensity (Brunner et al., 2021a). Besides the turbulence level, other conditions such as aspect ratio, measurement method, probe position, and the correction methods applied also contribute to these discrepancies (Tab. 2). For example, Brunner et al. (2021a) utilises midspan pressure taps for force calculation, while Jacobs (1931) measures the total force over the 3D airfoil. Also the AR is different, which significantly varies the force distribution along the span (Hammer et al., 2022; Ragni and Ferreira, 2016; Winkelman and Barlow, 1980).

https://doi.org/10.5194/wes-2026-155
Preprint. Discussion started: 9 September 2026

Overall, the measured data agree well with XFOIL under the fully turbulent assumption, except at and beyond stall onset. The minor deviation in the lift coefficients between the measurement and 2D-XFOIL can be seen in Fig. 4, in the linear region up to angle of attack of $\alpha \sim 10°$, the measured lift coefficients are lower than the 2D-XFOIL, as previously noted by Brunner et al. (2021a). 2D-XFOIL prediction shows delayed static stall with more gradual decrease in lift and increase in drag after the stall onset, resulting in higher lift and lower drag forces within the stall region $\alpha > \alpha_{\mathrm{ss}}$.

3.2 Aspect ratio AR = 0.25 and AR = 2.5

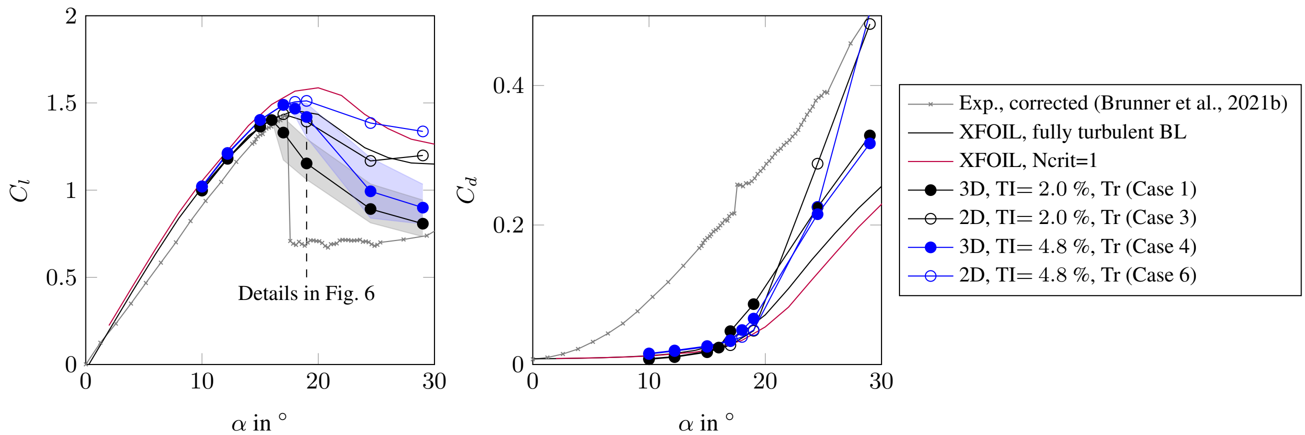

Figure 5. Lift and drag coefficients from Q3D URANS simulations with AR= 0.25 (2D) and 2.5 (3D) at TI= 2.0 % and 4.8 %. Shaded areas representing spanwise variation of the lift coefficient

Figure 5 shows the static polar from URANS simulations with a low AR of 0.25 (2D), and a high AR of 2.5 (3D) at turbulence intensity TI of 2.0% and 4.8%. In the attached flow region, there is no appreciable difference between the 2D-XFOIL results and both AR cases, verifying the suitability of the 2D approximation under these conditions. In the stall region, the URANS simulations with AR = 0.25 (2D) exhibit similar behaviour to XFOIL, both in terms of stall onset angle and stall type (trailing-edge stall). However, the magnitude of C_l following stall onset is slightly lower than that predicted by XFOIL, but remains higher than in the AR = 2.5 (3D) cases. For AR = 2.5 (3D), stall occurs approximately 1...2° earlier than in the 2D simulations, the onset is more abrupt, which is in closer agreement with the experimental data. Overall, the 3D cases demonstrate approximately 40% lower lift in the stall region compared to the 2D cases. This trend is consistent with the findings of Montalà et al. (2026), that the insufficient span length can lead to overpredictions of lift and drag in separated flow regions due to the induction of non-physical flow structures. In Fig. 5, the shaded regions denote significant spanwise variation in lift associated with the formation of three-dimensional stall cells (see the contour plots in Fig. 6).

Additionally, near and after the onset of static stall, an increase in lift is observed with increasing freestream turbulence intensity. This observation is in good agreement with the results from Huang et al. (2020) and Damiola et al. (2023), who

https://doi.org/10.5194/wes-2026-155
Preprint. Discussion started: 9 September 2026

WIND ENERGY SCIENCE DISCUSSIONS

demonstrated that increased turbulence intensity enhances flow reattachment and consequently increases lift near the stall region. This will be investigated in more detail using the DDES setup in a subsequent section of this paper.

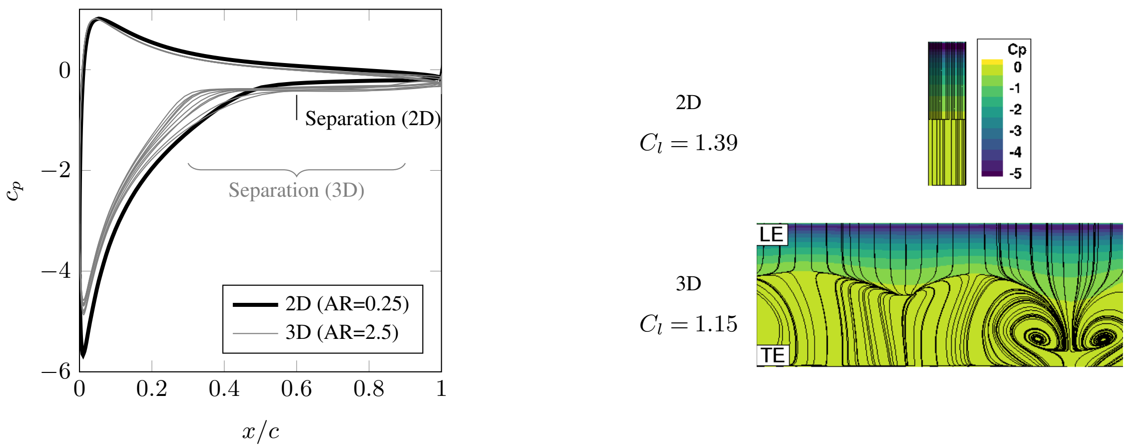

Figure 6. Pressure distribution c_p at 10 span positions (left) and snapshot of streamlines on the suction-side at $\alpha = 19°$ (after stall onset) from URANS simulations with TI$= 2.0$ % with AR$= 0.25$ (2D) and 2.5 (3D) (right)

Further details at $\alpha = 19°$ (beyond stall) comparing 2D and 3D cases are shown in Fig. 6. The pressure distribution shows no spanwise variation in the 2D case, as expected. In the 3D case, however, distinct difference is seen along the span, particularly in terms of the suction peak near LE and the separation position. In the 2D simulation, the suction peak is more pronounced than in the 3D case close to $c_p = -6$, and flow separation occurs further downstream at $x/c \sim 0.6$. In contrast, the 3D case exhibits strong spanwise variation in the separation point, mostly earlier ($x/c = 0.3...0.5$), but also extending much further downstream ($x/c \sim 0.9$), due to the spanwise extension of large-scale stall cells. These stall cells are highly unsteady, with both their position and size fluctuating over time.

As expected, no evidence of a laminar-turbulent transition can be identified in the pressure distribution c_p, e.g. a local plateau associated with laminar separation bubbles, since transition occurs very close to the leading-edge. Therefore, the fully turbulent assumption should be valid. Further details regarding the influence of transition model, supporting the aformentioned assumption, is found in Appendix B. All subsequent simulations are performed with AR $= 2.5$ without applying the transition model.

3.3 Comparison between URANS and DDES methods

Figure 7 shows the lift and drag coefficients from URANS and DDES simulations for freestream turbulence intensities of 2.0 % and 4.8 %. In the attached flow region up to the stall onset, both URANS and DDES predict nearly identical results, including the stall onset angle for a given turbulence intensity. However, the stall characteristics are different: DDES predicts a more abrupt stall similar to the experiments. In addition, the spanwise variation (shaded area) is notably larger in DDES cases

https://doi.org/10.5194/wes-2026-155
Preprint. Discussion started: 9 September 2026

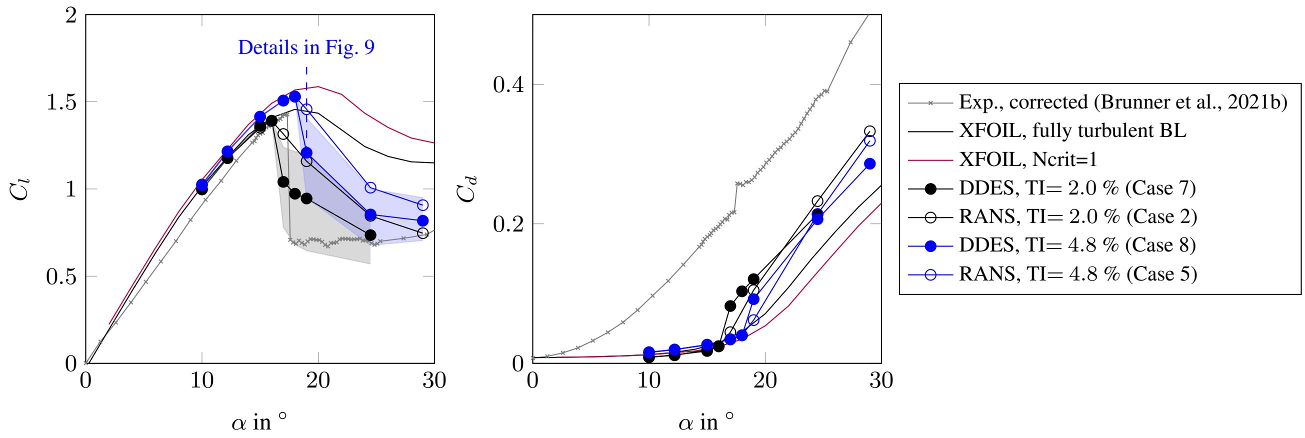

Figure 7. Comparison between RANS and DDES results at TI $= 2.0$ % and 4.8 %. Shaded areas representing spanwise variation of the lift coefficients

compared to URANS cases (shown in Fig. 5). This difference is distinct immediately after stall onset, but becomes smaller in the fully separated region (deep-stall near $\alpha = 30°$).

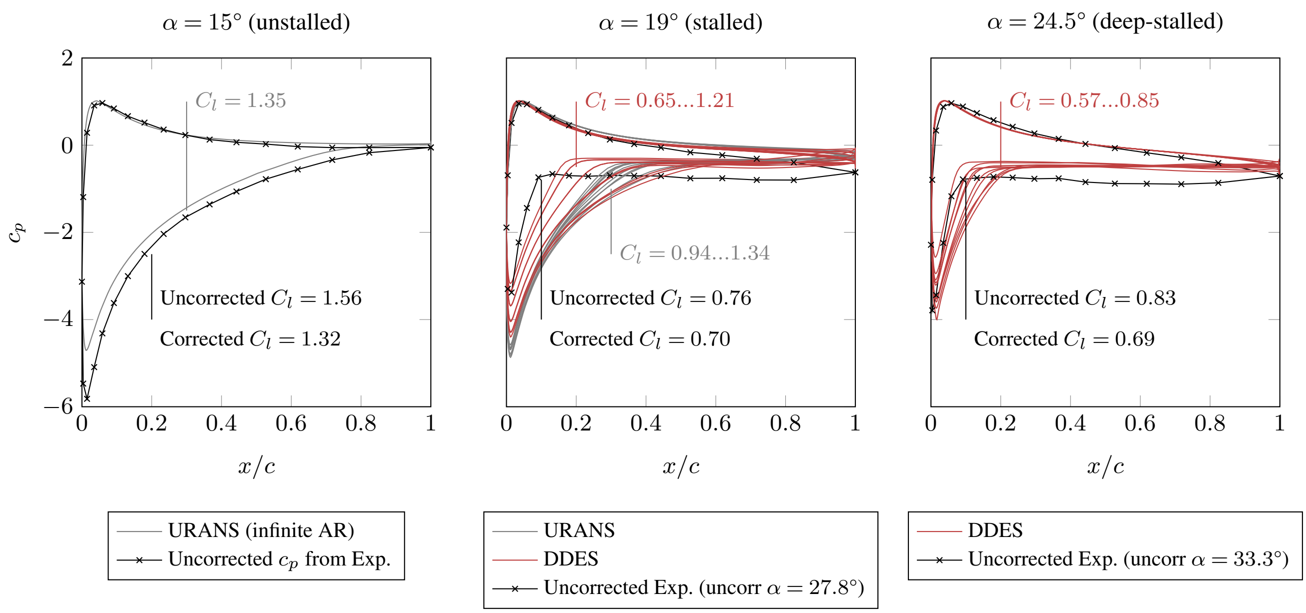

Figure 8. Pressure distribution c_p at $\alpha = 15°$ (unstalled region), $\alpha = 19°$ (stalled region), and $\alpha = 24.5°$ (deep-stalled region) from experiment Brunner et al. (2021b), URANS, and DDES simulations with TI= 2.0 %. Uncorrected c_p measurement at midspan of AR=1.5 airfoil from the experiment, while c_p extracted at 10 spanwise positions from simulations

https://doi.org/10.5194/wes-2026-155
Preprint. Discussion started: 9 September 2026

The differences in stall onset behaviour are further analysed in the pressure distributions c_p (Fig. 8) and flow streamlines (Fig. 9a). It should be noted that both corrected and uncorrected lift coefficient C_l are provided from the experimental dataset (Brunner et al., 2021a, b) for both angle of attack and freestream velocity due to wind tunnel blockage, but c_p is not corrected. This is evident in Fig. 8 at $\alpha = 15°$, where the corrected measured $C_l = 1.32$ is lower than the URANS simulation ($C_l = 1.35$), but the area from the local c_p curve is larger from the measurement with uncorrected $C_l = 1.56$. The finite AR in closed wind tunnel tests primarily affects the suction-side (see LES results from Haase et al. (2010)), resulting in a deeper negative suction peak compared to simulations assuming farfield boundary conditions. At $\alpha = 19°$, URANS predicts flow separation mostly around mid-chord ($x/c = 0.3...0.5$) across the span, whereas the DDES case shows partially much earlier separation, starting from near the maximum thickness ($x/c \sim 0.2$), forming larger stall cells (chordwise and spanwise extension of stall cells in Fig. 9a). The earlier separation from the measurement at $x/c = 0.1$ can be again attributed to the low AR and confined wind tunnel cross section. The deviation between DDES simulation and experiment becomes smaller in the fully separated region ($\alpha = 24.5°$), the separation point between experiment and DDES simulation is in a good agreement at $x/c = 0.1$.

In Fig. 9b and 9c, the contours are shown at the spanwise position corresponding to the maximum separation, i.e., the centers of the stall cells. The DDES captures the large static stall and trailing vortices, while URANS shows enhanced flow attachment and thus smaller vortices (Fig. 9b). Compared to DDES, the URANS setup overpredicts the turbulent kinetic energy k within the separated flow region, e.g. vortex core and high shear region between stall vortex and trailing-edge vortex (Fig. 9c). In contrast, the DDES setup shows high turbulent kinetic energy primarily at the outer region of each vortex where high shear stresses are expected. In addition to k, further differences between URANS and DDES are observed in the potential flow region downstream of the airfoil. The red area in Fig. 9d indicates the areas where the LES mode is activated within the DDES simulation. As expected, the boundary layer region remains Reynolds-averaged (blue), such that no significant differences between URANS and DDES are expected in the prediction of boundary layer separation itself. Instead, flow separation is influenced by the potential flow field both upstream and downstream of the airfoil, where the LES mode is activated. Upstream of the airfoil, the DES simulation induces greater flow turning around the leading-edge, resulting in a locally increased effective angle of attack. This induces a more abrupt flow separation compared to URANS. Downstream of the airfoil, the DDES setup resolves larger eddies and a higher adversed pressure gradient, further increasing the effective angle of attack, triggering earlier separation. This mechanism more closely resembles the physical phenomena observed in experiments.

Further characteristics of the stall vortices are investigated by spectral analysis. Figure 10 shows the spectra from URANS and DDES simulations at multiple angle of attack: attached region ($\alpha = 12.2°$), directly before stall onset ($\alpha = 18°$), directly after stall onset ($\alpha = 19°$), and deep-stall ($\alpha = 24.5°$). From URANS simulation, only the very low frequency region shows higher energy directly after the stall onset, indicating limited unsteady behaviour. In contrast, DDES shows the typical spectra of stall vortices after stall onset ($\alpha > 19°$): the unsteady energy is increased across a broad range of frequencies in the stalled region ($\alpha > 19°$). A distinct spectral peak and its higher harmonics emerge at a reduced frequency of $f^* = 0.11$ immediately after stall onset ($\alpha = 19°$); this frequency reduces to $f^* = 0.08$ in deep stall ($\alpha = 24.5°$), consistent with the enlarged dimension of vortex structure. In the context of wind turbines at 90° angle of attack, the vortex shedding frequency is typically $St =$

https://doi.org/10.5194/wes-2026-155
Preprint. Discussion started: 9 September 2026

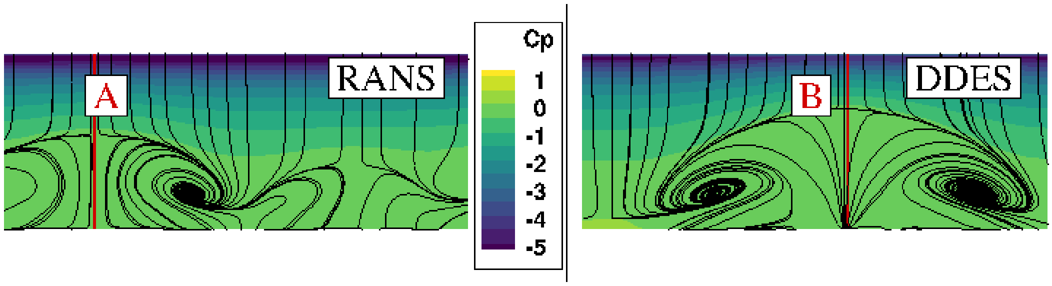

(a) Pressure distribution and streamlines on airfoil suction-side with maximum separation locations marked in red

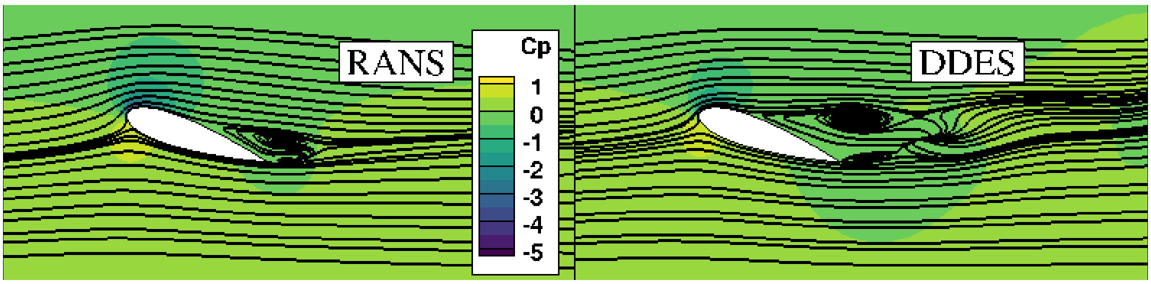

(b) Pressure distribution and streamlines at plane A and B from Fig. 9a

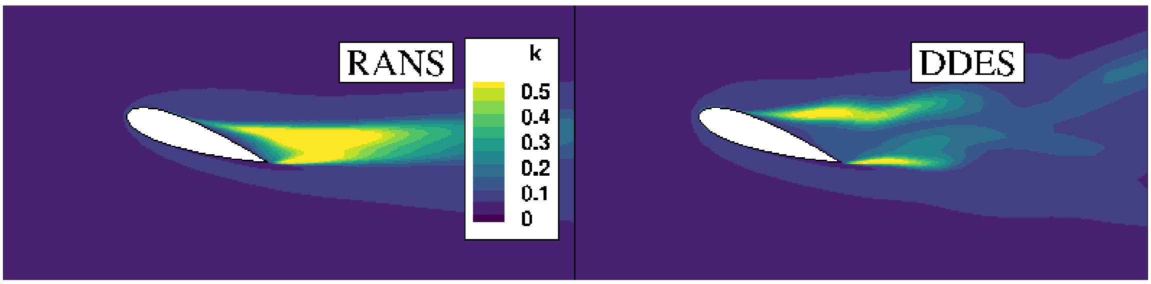

(c) Turbulent kinetic energy at plane A and B

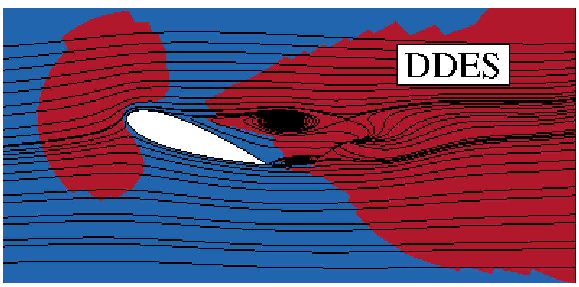

(d) LES region in DDES setup (red: LES, blue: RANS)

Figure 9. Instantaneous flow field from URANS, Case 5 (left) and DDES, Case 8 (right) at stalled condition of $\alpha = 19°$ with TI$= 4.8$ %

$fL/U_\infty \sim 0.1 \ldots 0.15$ (summary from Fernandez-Aldama et al. (2025) at Re=2×10^6). These observations confirm the capability

https://doi.org/10.5194/wes-2026-155
Preprint. Discussion started: 9 September 2026

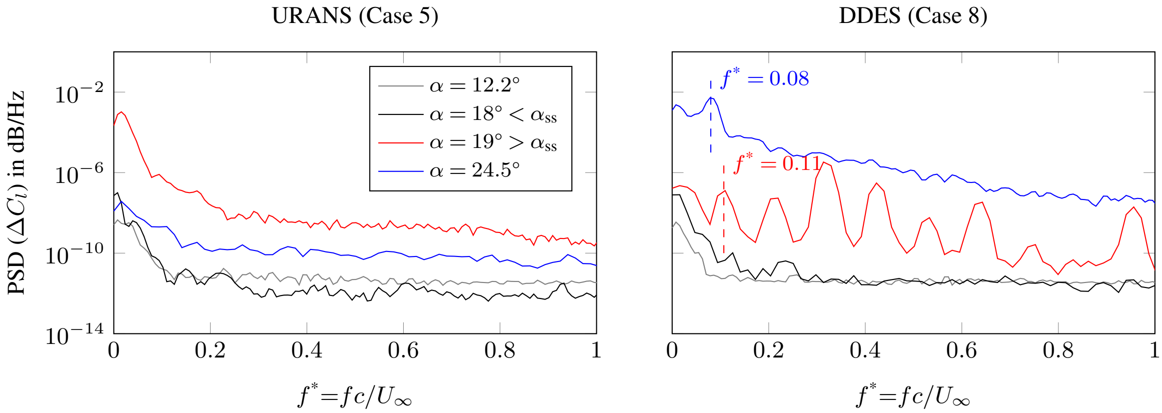

Figure 10. Spectra of unsteady lift at static conditions with URANS and DDES for TI= 4.8 % from various angle of attack. Static stall onset at $18° < \alpha_{ss} < 19°$

of the DDES approach to capture the dominant dynamics of stall cell formation, while the standard URANS approach fails to resolve it accurately.

4 Influence of Turbulence Intensity on Static Stall

285 Figure. 11a shows the effect of varying inflow turbulence intensities (TI) on lift and drag coefficients, calculated with DDES setup. With increasing TI, the onset of static stall is systematically delayed (aee also Fig. 11b), the stall onset angle changes by up to 3° over the range $0.5\% < \text{TI} < 9.6\%$. This finding is consistent with previous studies from Huang et al. (2020); Damiola et al. (2023), that higher turbulence intensity delays stall onset. Not only the onset angle, but also the stall type is changed: the abrupt lift drop at low TI gradually develops into moderate trailing-edge stall. This stall delay can be attributed to enhanced 290 flow mixing near the boundary layer, which improves flow attachment.

For cases with freestream turbulent intensity below 2.0%, the results are nearly different. At TI=3.6%, the lift curve initially follows that of the TI=2.0% case, but the stall onset is further delayed. For TI $> 4.8\%$, the lift curve begins to deviate already in the attached flow region, starting at $\alpha = 15°$, exhibiting higher lift compared to lower TI cases, following along XFOIL curve with the free transition case. At TI=9.6%, the stall onset is further delayed and the characteristic abrupt lift drop does not occur. 295 From these results, a distinct change in stall characteristics occurs around TI=4% for the cases studied. The case with TI=3.6% agrees the best with experimental data in terms of stall onset angle, despite the far upstream wind tunnel turbulence level being reported in the range of $0.3...1.1\%$ (Kiefer et al., 2022).

https://doi.org/10.5194/wes-2026-155
Preprint. Discussion started: 9 September 2026

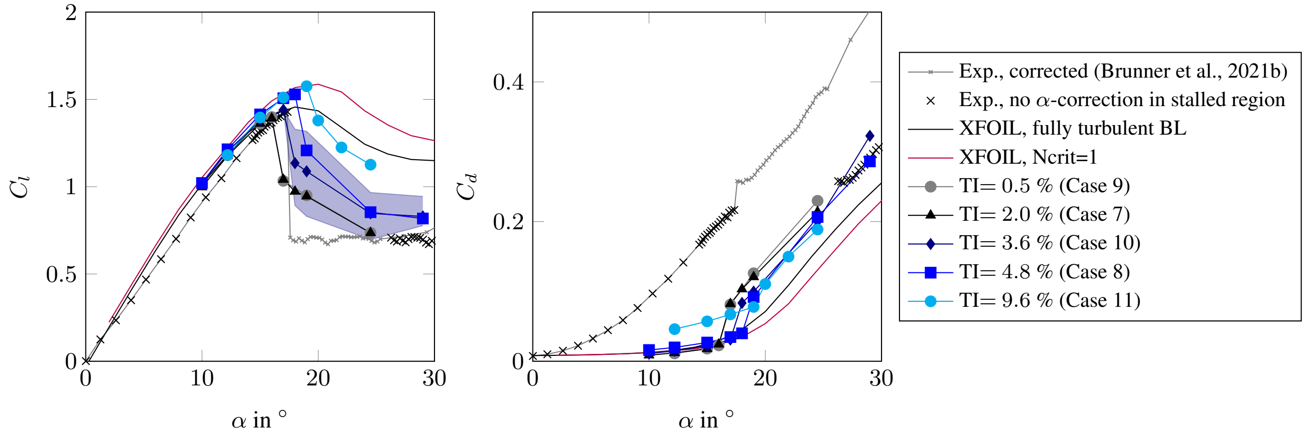

(a) Lift and drag coefficients. Shaded area representing spanwise variation for TI= 3.6 % (Case 10)

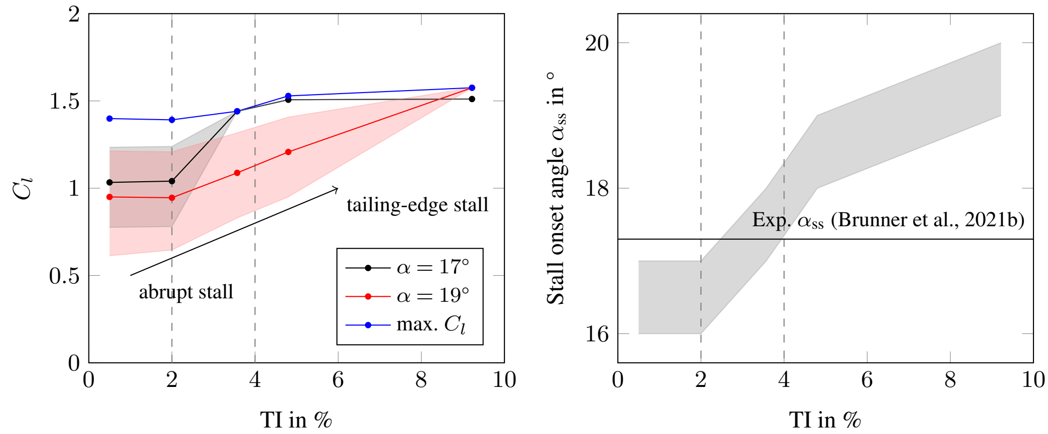

(b) Lift coefficient and static stall onet angle in turbulence intensity: Indifference below TI= 2.0 % and, characteristic change at TI∼ 4 %

Figure 11. Influence of inflow turbulence intensity on static polar from DDES simulations

5 Dynamic Stall

5.1 Influence of inflow turbulence intensity

Figure 12 shows the lift and drag coefficients in time during pitching-up settings over the ranges of the angle of attack of 12.2...20.3°, and 12.2...25.2°. The pitching starts at $t^* = 0$ and ends at $t^* = 15.3$. Experimental reference data from Kiefer et al. (2022) correspond to pitching between uncorrected angle of attack of 19...29°. In addition to the uncorrected coefficients (C_l and C_d) from Kiefer et al. (2022), the figure also shows the corrected coefficients, accounting for increased freestream velocity induced by wind tunnel blockage, following the appoach of Brunner et al. (2021a). It should be noted again that the application of these corrections to both angle of attack and force coefficients under transient conditions, especially post-stall region, is not yet validated in the literatures. Furthermore, the coefficients from the experiment are measured at midspan within

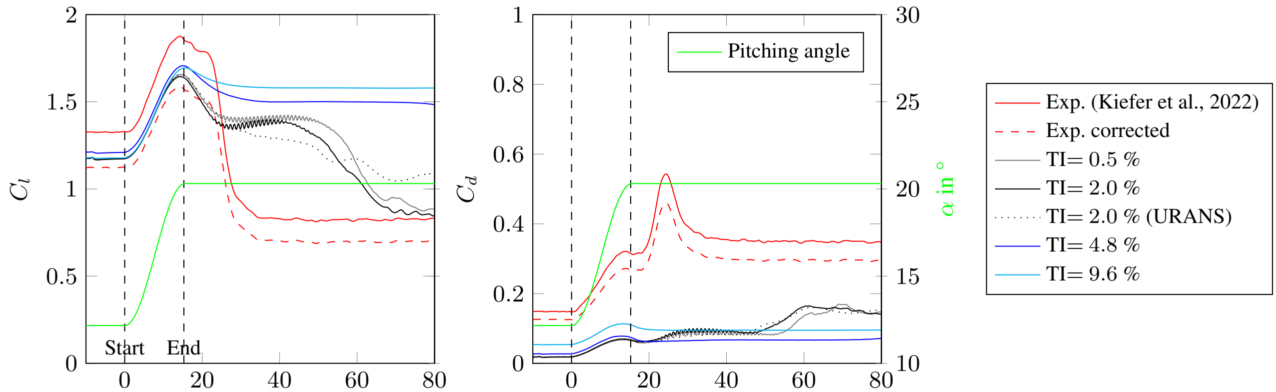

(a) Pitching A: 12.2° to 20.3°

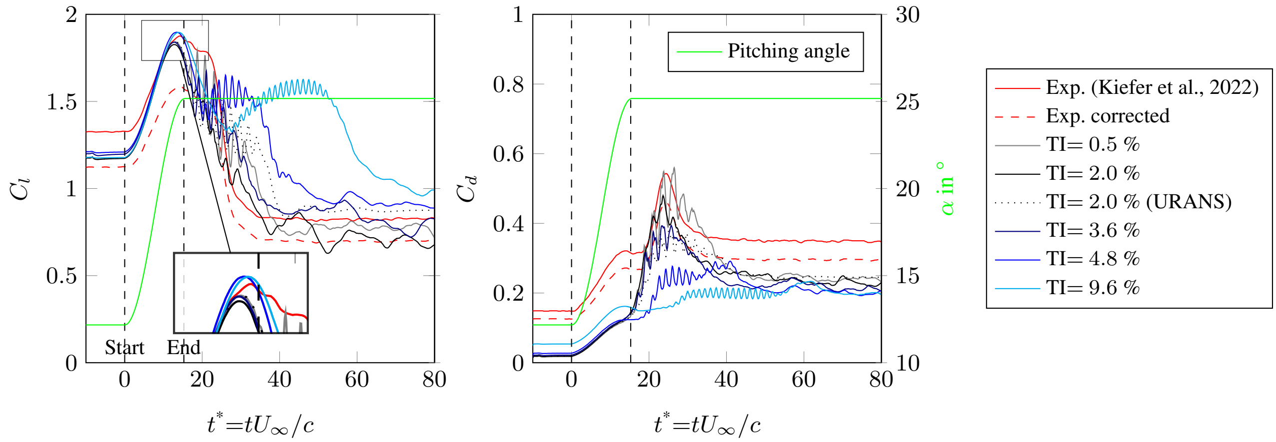

(b) Pitching B: 12.2° to 25.2°

Figure 12. Lift and drag coefficients during dynamic pitching from DDES simulations for different freestream turbulence intensities

a finite span (AR=1.5), while they are area-averaged over the span from the simulations as the infinite span is assumed with periodic boundary conditions.

From Fig. 12a, the DDES simulations at low turbulence intensity (TI $< 2\%$) closely match the corrected experiment lift coefficient up to $t^* = 25$, which includes both the pitch-up phase and the early post-stall region. After $t^* \sim 30$, the experimental lift rapidly converges to the static stall value at $\alpha = 20.3°$, while the simulations require a much longer time until $t^* = 70$ to reach the convergence. This discrepancy may be attributed to the finite span of the airfoil in the experiment, allowing a stall cell to rapidly stabilise at midspan, while in the simulation with effectively infinite span, the formation and development of dynamic stall cells is more spatially distributed and temporally extended. Alternatively, the difference could also result from inadequacies in the correction applied to the experimental data under transient conditions. For the Pitching B in Fig. 12b, where the airfoil is pitched up into the deep-stall regime, the convergence of the lift coefficient in the DDES simulations is

https://doi.org/10.5194/wes-2026-155
Preprint. Discussion started: 9 September 2026

faster than for Pitching A. In the post-stall region $15 < t^*$, good agreement is observed between the experimental data and simulation results. The sudden peak in the drag coefficient C_d within this region $20 < t^* < 30$ is accurately captured under the Pitching B condition at low freestream turbulence intensity. The post-stall phase is characterised by high fluctuations in both lift and drag at distinct frequencies, especially immediately after reaching the maximum pitching angle at $t^* = 15.3$. The dominant fluctuation frequency is significantly higher than that associated with static stall vortices, which is the decaying characteristics of dynamic stall vortices (DSV).

The sensitivity to inflow turbulence intensity during dynamic stall under the pitching-up conditions is not as distinct as for static stall. The dominant factor influencing the lift increase appears to be the momentum associated with the pitching motion itself, while the influence of enhanced boundary-layer mixing due to increased freestream turbulence intensity is relatively minor. Although two characteristic groups can be identified with a threshold at TI =4%, the effect of turbulence intensity is less evident in terms of the maximum lift peak. However, in the post-stall region, different characteristics are seen for higher turbulence intensities (TI >4%): the convergence toward the static stall state is delayed. This effect is even more pronounced in the drag coefficient, where the drag peak observed at low turbulence intensities in Pitching B does not occur under highly turbulent conditions. These findings are consistent with previous studies from Huang et al. (2020); Damiola et al. (2023), that the dynamic stall is less sensitive to the turbulent condition during the up-pitching.

5.2 Spectral analysis

A frequency analysis is conducted to understand the decaying behaviour of the dynamic stall vortices, as these structures have the potential to induce vortex-induced vibrations. The analysis procedure is as follows:

1. The simulation employs a variable time step controlled by the maximum CFL number; therefore, the data are first resampled at a fixed sampling frequency.

2. To extract the fluctuating component of the signal, its temporal average—calculated using a moving average over a defined window size—is subtracted from the original signal.

3. The time–frequency representation (spectrogram) is then obtained with 90% window overlap.

The choice of window size is the compromise between frequency resolution and the ability to capture transient behaviour. This analysis setup is sufficient to identify the dominant frequencies associated with dynamic stall vortices, enabling quantitative comparison between different simulation cases.

Figure 13 shows the spectrogram for the Pitching B case. During the pitching-up ($0 < t^* < 15.3$), no distinct spectral peaks are observed, as the rapid motion prevents the formation of coherent stall vortices yet. The high energy area at frequency $f^* \sim 0.1$ is subject to high uncertainty due to the small window size used in the individual FFT analyses. After reaching the maximum angle of attack, finishing the up-pitching motion at $t^* > 15.3$, distinct peaks appear at $f^*_{\mathrm{ds}} \sim 0.5$ and its higher harmonics ($2f^*_{\mathrm{ds}}$ and $3f^*_{\mathrm{ds}}$). These frequencies are much higher than those observed for static stall at $f^*_{\mathrm{ss}} \sim 0.1$ (see Fig 10), implying that dynamic stall vortices are associated with smaller spatial and temporal scales compared to static stall vortices.

https://doi.org/10.5194/wes-2026-155
Preprint. Discussion started: 9 September 2026

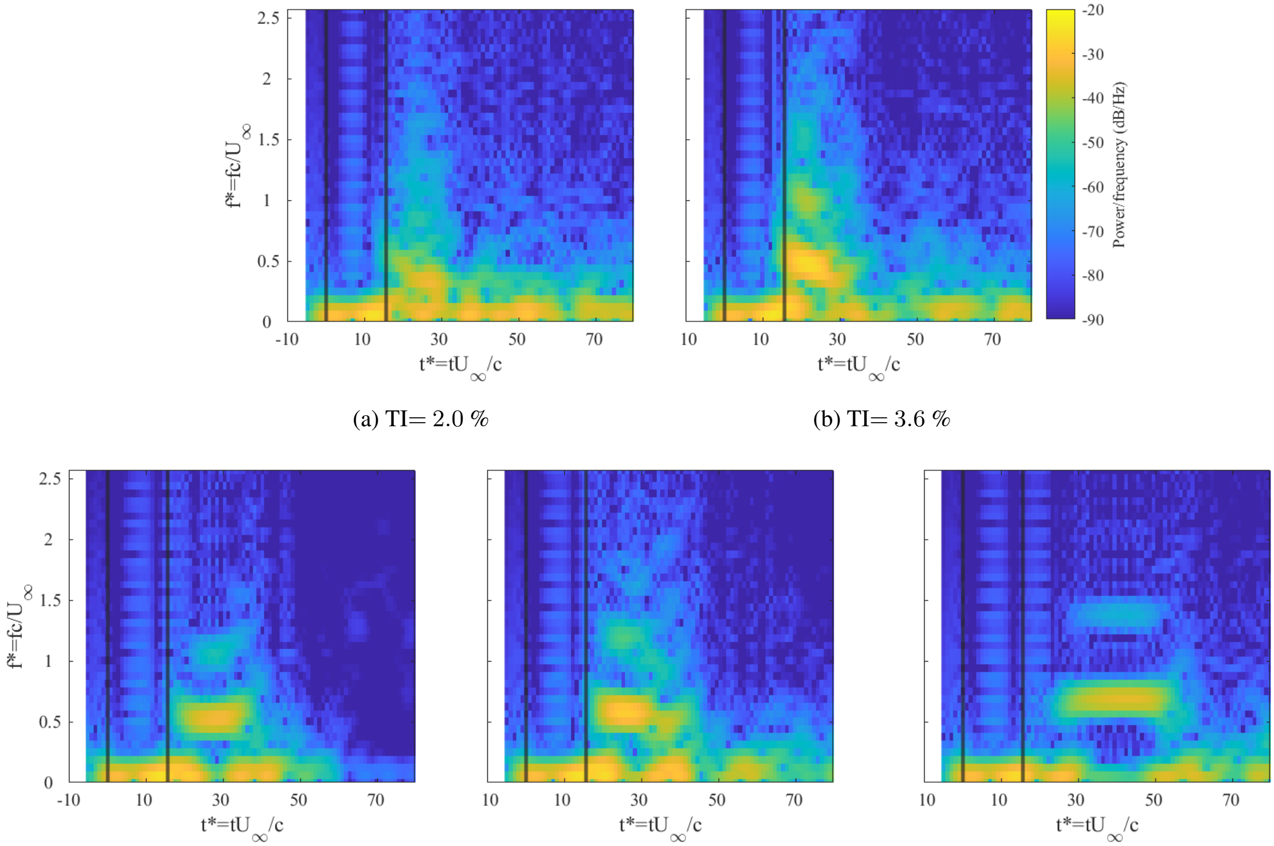

(a) TI= 2.0 %

(b) TI= 3.6 %

(c) TI= 4.8 % (URANS)

(d) TI= 4.8 %

(e) TI= 9.6 %

Figure 13. Spectrogram of lift coefficients from dynamic pitching simulations for Pitching B 12.2° to 25.2°, using DDES setups with different freestream turbulence intensities

The high frequency excitation induced by dynamic stall is consistent with experimental observations described in Fouest et al. (2021), where, following a step-up pitching motion at Re$= 0.75 \times 10^6$, an initial high frequency (St~ 1.8) is excited, which later settles to St~ 0.2 a typical vortex shedding frequency of static stall. The frequency of the dynamic stall vortices, f^*_{ds}, tends to increase with higher freestream turbulence intensities. For TI=3.6%, the dynamic stall vortices start decaying immediately after the up-pitching motion is finished at $t^* = 15.3$. At $t^* > 40$, these vortices are fully dissipated, leaving only static stall vortices. The decay process becomes increasingly slow as turbulence intensity increases.

A comparison between URANS (Fig. 13c) and DDES (Fig. 13d) at TI=4.8% shows only minor differences up to $t^* = 30$. However, the DDES simulation shows a more diversified frequency spectrum between $t^* = 30...50$, suggesting that DDES resolves decaying process more refined. In addition to that, URANS is not able to resolve the static stall at $t^* > 50$, as previously discussed in Fig. 10.

https://doi.org/10.5194/wes-2026-155
Preprint. Discussion started: 9 September 2026

6 Conclusions and Outlook

Using URANS and DDES methods, the static and dynamic stall behaviour dependent on the freestream turbulence intensity is analysed in this paper. The conclusions are as follows:

- At a Reynolds number of 5.5×10^6, flow over an airfoil can be assumed to be fully turbulent.
- 2D and Q3D simulations with small aspect ratios are insufficient to accurately predict stall onset and post-stall behaviour. 3D simulations with a large aspect ratio (ideally, greater than twice the chord) are necessary to fully resolve large spanwise stall cells, which can extend the length-scale of higher than one chord length.
- URANS simulations are adequate to predict the onset angle of both static and dynamic stall, however lack the accuracy for the post-stall performance. Due to the artificial viscosity generated by turbulence models, the flow upstream and downstream of the airfoil during the stall, especially the stagnation point and the downstream pressure field is falsely predicted. DDES simulations, in contrast, are capable of resolving large eddies near the airfoil, especially the stalled region on the suction-side downstream, enabling accurate prediction of abrupt stall characteristic. DDES also captures periodic stall vortices with a reduced frequency $\mathrm{St} \sim 0.1$, which potentially induce rotor vibrations. Importantly, the DDES setup utilised in this study requires negligible increase of the computational cost compared to URANS setup.
- The inflow turbulence intensity has a significant impact on airfoil performance near the static stall regime (pre/onset/post-stall). Increasing turbulence intensity delays stall onset, reaching a higher maximum lift coefficient. Additionally, the abrupt decrease in lift after stall onset becomes moderate with increased freestream turbulence. The characteristic change occurs at 4 % of freestream turbulence intensity for the cases studied in this work.
- However, inflow turbulence intensity has negligible influence on the change in lift coefficient during dynamic pitching of the airfoil. The momentum of the pitching airfoil is higher than that of the turbulent freestream. Only in the post-stall region, after the dynamic pitching-up, is influenced, as highly turbulent freestream enhances flow mixing and delays complete detachment of the flow.

Based on the findings, the following future works are suggested.

- The wind tunnel correction method requires validation in the stall regime. Systematic numerical studies should be conducted to estimate the influence of aspect ratio, end-wall effects, and wind tunnel contraction on the stalled flow. Simulating a finite airfoil with surrounding walls may be computationally more expensive and more importantly, unrealistic for wind turbine rotors, this should verify the correction method of the experimental data in stalled flow conditions.
- Rather than specifying inflow turbulence as integral quantities, spectral inflow conditions should be considered as inflow boundary conditions in DDES simulations.
- Comprehensive sensitivity analyses of turbulence models could be pursued. For example, recalibration of the coefficients in the SST model could improve predictions of flow turning and mixing near the leading and trailing edges in fully

https://doi.org/10.5194/wes-2026-155
Preprint. Discussion started: 9 September 2026

modelled URANS simulations. The impact of such recalibration on DDES predictions should also be examined. While LES remains expensive at these Reynolds numbers, other hybrid approaches—such as improved Delayed Detached-Eddy Simulation (iDDES) or alternative near-wall turbulence models—should be considered.

- Further validation of DDES approach including the influence of turbulence intensity on stall behaviour can be studied at higher Reynolds numbers towards Re$= 15 \times 10^6$ for non-symmetric, optimised airfoils, e.g. DU or FFA groups, if the measurement data is available.

- The DDES results should be utilised to verify and improve the accuracy of low-order models, such as those based on blade element theory or the vortex lattice method.

Data availability. The simulations data could be supplied upon request.

Appendix A: Mesh Study

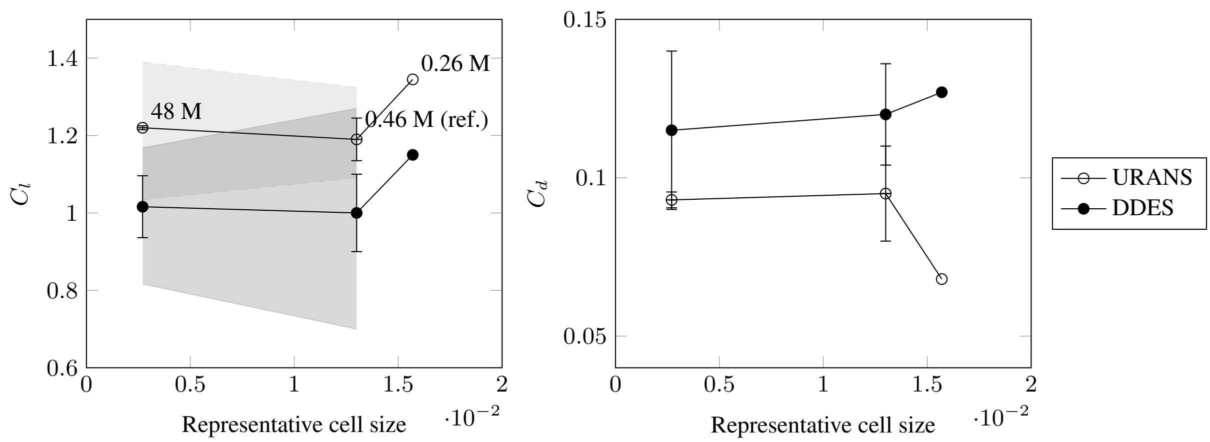

Figure A1. Mesh study at $\alpha = 19°$ for TI=2.0%. Error bar indicating timely fluctuation, shared region indicating spanwise variation

The mesh study is performed at $\alpha = 19°$ (stalled condition) and TI$= 2.0$ %, where large stall cells are observed. These conditions correspond to a decrease in the overall lift coefficient, yet prior to entering deep-stall region characterised by full flow separation. The total number of cells of 0.26×10^6 (coarse), 0.46×10^6 (reference), and 48×10^6 (fine) are simulated for both URANS and DDES setups. For all grids, y+ is kept below 1, only x+ and z+ were varied.

Figure A1 shows the lift and drag coefficients in representative cell size for 3 cases. Error bars indicate the maximum amplitude of the fluctuations in simulation time, while the shared region illustrates the spanwise variation in the lift coefficient. The reference to fine GCI is 0.01% for the URANS setup and even lower for the DDES setup, although they show oscillatory

https://doi.org/10.5194/wes-2026-155
Preprint. Discussion started: 9 September 2026

convergence. Although it shows an acceptable convergence at the reference cell size for the averaged C_l and C_d, the temporal fluctuation (error bar) and the spanwise fluctuation (shaded area) certainly deviate between the reference and fine cases. This suggests that the reference mesh is acceptable for the analysis of the static polar, however, for the quantitative evaluation of transient behaviour, e.g. amplitude of stall vortices relevant to FSI simulation, a finer mesh might be required.

Appendix B: Influence of Transition Model

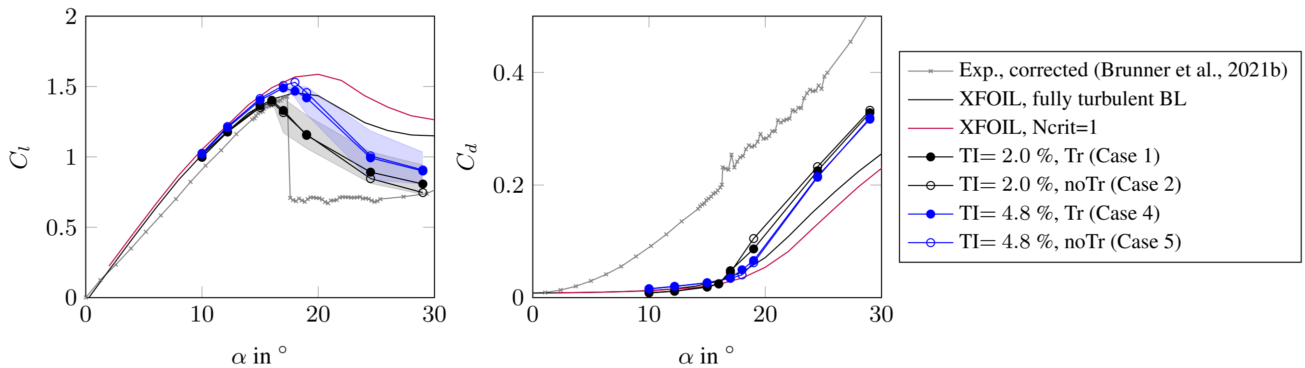

Figure B1. URANS simulations with and without transition model at TI= 2.0 % and 4.8 % for AR=2.5. Shared areas representing spanwise variations from the cases with transition model

Figure B1 shows the influence of the $\gamma - \mathrm{Re}_\theta$ transition model on the prediction of static polar. URANS simulations were performed at two different freestream turbulence intensities of $\mathrm{TI} = 2.0$ % and 4.8 % with the $\mathrm{AR} = 2.5$ setup. Comparing the results obtained with and without the transition model (solid and hollow symbols, respectively), almost no difference, except for a deviation near stall at $\alpha = 18°$, is observed at the high turbulence intensity of TI=4.8 %. This results confirms the validity of the fully turbulent assumption around the airfoil at this high Reynolds number (5.5×10^6), as experimentally shown by Kiefer et al. (2022).

Appendix C: Influence of Aspect Ratio (AR) and Wall Effects

The reference setup used in this study is $\mathrm{AR} = 2.5$ with translational periodic boundary conditions in the spanwise direction. To further investigate the influence of AR and end-wall effects, two additional simulations were performed: one employing $\mathrm{AR} = 2.5$ with slip-wall boundary conditions to constrain the flow, and another with $\mathrm{AR} = 1.5$, also utilising slip-walls. Figure C1 shows the lift and drag coefficients at $\alpha = 19°$ (stalled region) obtained from the experiment (Brunner et al., 2021b) and the DDES simulations with varying AR and wall boundary conditions. The error bars indicate spanwise variations. It should be noted that the slip-wall boundary condition used in the simulations is not exactly identical to the experimental setup, and the area-integrated forces in the simulations are not directly comparable to the mid-span measurements from the

https://doi.org/10.5194/wes-2026-155
Preprint. Discussion started: 9 September 2026

experiments. The results indicate that both a smaller aspect ratio and the presence of side walls decrease the lift and increase the drag coefficient. The discrepancies between the experimental results and the DDES simulations may be partly attributable to the low aspect ratio (AR $= 1.5$) used in the experiment. In particular, the relatively high drag coefficient observed in the experimental data can likely be explained by the influence of the walls.

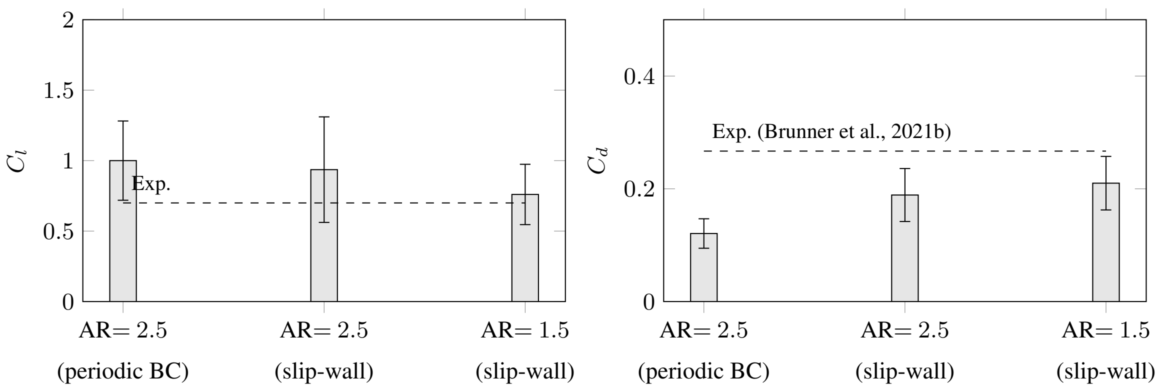

Figure C1. Influence of aspect ratio (AR) and boundary conditions on the side walls at $\alpha = 19°$ using DDES setup with TI=2.00%. Error bars representing the spanwise variation

430 *Author contributions.* Hye Rim Kim conducted the numerical simulations and analysis, and wrote the manuscript under the supervision from Lars Wein.

Competing interests. The authors declare that no cometing interest are present.

Acknowledgements. The authors would like to acknowledge the German Research Foundataion (DFG, Deutsche Forschungsgemeinschaft) for the funding of the Collaborative Research Center (CRC) 1463 "Integrated design and operation methodology for offshore megastructures".
435 The cluster and storage system supplied by the Scientific Computing at the Leibniz University IT Servies (LUIS) are greatly appreciated.

https://doi.org/10.5194/wes-2026-155
Preprint. Discussion started: 9 September 2026

eawe european academy of wind energy
Open Access WIND ENERGY SCIENCE DISCUSSIONS

References

Athkuri, S. S. C., Nived, M. R., Aswin, R., and Eswaran, V.: Static-stall prediction of airfoils at high Reynolds numbers using hybrid RANS–LES models, The European Physical Journal Special Topics, https://doi.org/10.1140/epjs/s11734-025-01771-0, 2026.

Brunner, C. E., Kiefer, J., Hansen, M. O., and Hultmark, M.: Study of Reynolds number effects on the aerodynamics of a moderately thick airfoil using a high-pressure wind tunnel, Experiments in Fluids, 62, 1–17, 2021a.

Brunner, C. E., Kiefer, J., Hansen, M. O. L., and Hultmark, M.: Static measurements of a NACA 0021 airfoil at high Reynolds numbers, https://doi.org/10.34770/9mv0-zd78, 2021b.

Ceyhan, O., Pires, O., Munduate, X., Sorensen, N. N., Schaffarczyk, A. P., Reichstein, T., Diakakis, K., Papadakis, G., Daniele, E., Schwarz, M., Lutz, T., and Prieto, R.: Summary of the Blind Test Campaign to predict the High Reynolds number performance of DU00-W-210 airfoil, https://doi.org/10.2514/6.2017-0915, 2017.

Chellini, S., De Tavenier, D., and Von Terzi, D.: Impact of dynamic stall model tailoring on wind turbine loads and performance prediction, Journal of Physics: Conference Series, 2767, 022 016, https://doi.org/10.1088/1742-6596/2767/2/022016, 2024.

Chellini, S., De Tavernier, D., and von Terzi, D.: Experimental characterization of dynamic stall of the FFA-W3-211 wind turbine airfoil, Wind Energy Science, 11, 753–769, https://doi.org/10.5194/wes-11-753-2026, 2026.

Damiola, L., Siddiqui, M. F., Runacres, M. C., and De Troyer, T.: Influence of free-stream turbulence intensity on static and dynamic stall of a NACA 0018 aerofoil, Journal of Wind Engineering and Industrial Aerodynamics, 232, 105 270, https://doi.org/doi.org/10.1016/j.jweia.2022.105270, 2023.

Fernandez-Aldama, R., Papadakis, G., Lopez-Garcia, O., Avila-Sanchez, S., Riziotis, V. A., Cuerva-Tejero, A., and Gallego-Castillo, C.: Characterization of vortex-shedding regimes and lock-in response of a wind turbine airfoil with two high-fidelity simulation approaches, Wind Energy Science, 10, 17–39, https://doi.org/10.5194/wes-10-17-2025, 2025.

Fouest, S. L., Deparday, J., and Mulleners, K.: The dynamics and timescales of static stall, Journal of Fluids and Structures, 104, 103 304, https://doi.org/https://doi.org/10.1016/j.jfluidstructs.2021.103304, 2021.

Gaertner, E., Rinker, J., Sethuraman, L., Zahle, F., Anderson, B., Barter, G., Abbas, N., Meng, F., Bortolotti, P., Skrzypinski, W., Scott, G., Feil, R., Bredmose, H., Dykes, K., Shields, M., Allen, C., and Viselli, A.: Definition of the IEA 15-Megawatt Offshore Reference Wind Turbine, National Renewable Energy Laboratory (NREL), 2020.

Gross, A., Fasel, H. F., and Gaster, M.: Criterion for Spanwise Spacing of Stall Cells, AIAA Journal, 53, 272–274, https://doi.org/10.2514/1.J053347, 2015.

Haase, W., Braza, M., and Revell, A.: DESider – A European Effort on Hybrid RANS-LES Modelling, Springer Berlin, Heidelberg, https://doi.org/doi.org/10.1007/978-3-540-92773-0, 2010.

Hammer, P. R., Garmann, D. J., and Visbal, M. R.: Effect of Aspect Ratio on Finite-Wing Dynamic Stall, AIAA Journal, 60, 6581–6593, https://doi.org/10.2514/1.J062109, 2022.

Hansen, M. H., Gaunaa, M., and Aagaard Madsen, H.: A Beddoes-Leishman type dynamic stall model in state-space and indicial formulations, 2004.

Huang, X., Albers, M., Meysonnat, P., Meinke, M., and Schröder, W.: Analysis of the effect of freestream turbulence on dynamic stall of wind turbine blades, International Journal of Heat and Fluid Flow, 85, 108 668, 2020.

Jacobs, E. N.: Tests of Six Symmetrical Airfoils in the Variable Density Wind Tunnel, Tech. rep., National Advisory Committee for Aeronautics, 1931.

Kiefer, J., Brunner, C. E., Hansen, M. O., and Hultmark, M.: Dynamic stall at high Reynolds numbers induced by ramp-type pitching motions, Journal of Fluid Mechanics, 938, 2022.

Kim, H. R., Printezis, J. A., Ahrens, J. D., Seume, J. R., and Wein, L.: Characterization of dynamic stall of a wind turbine airfoil with a high Reynolds number, Wind Energy Science, 10, 161–175, https://doi.org/10.5194/wes-10-161-2025, 2025a.

Kim, H. R., Schwarzer, D., and Wein, L.: Parameter Study of Dynamic Stall under High Reynolds Numbers, in: 16th European Conference on Turbomachinery Fluid dynamics Thermodynamics, https://doi.org/https://doi.org/10.29008/ETC2025-178, 2025b.

Kosović, B., Basu, S., Berg, J., Berg, L. K., Haupt, S. E., Larsén, X. G., Peinke, J., Stevens, R. J. A. M., Veers, P., and Watson, S.: Impact of atmospheric turbulence on performance and loads of wind turbines: knowledge gaps and research challenges, Wind Energy Science, 11, 509–555, https://doi.org/10.5194/wes-11-509-2026, 2026.

Ladson, C. L.: Effects of Independent Variation of Mach and Reynolds Numbers on the Low-Speed Aerodynamic Characteristics of the NACA 0012 Airfoil Section, Tech. rep., NASA Langley Research Center, 1988.

Langtry, R. B. and Menter, F. R.: Correlation-Based Transition Modeling for Unstructured Parallelized Computational Fluid Dynamics Codes, AIAA Journal, 47, 2894–2906, https://doi.org/10.2514/1.42362, 2009.

Leishman, J. G. and Beddoes, T.: A Semi-Empirical model for dynamic stall, Journal of the American Helicopter society, 34, 3–17, 1989.

Menter, F. R.: Two-equation eddy-viscosity turbulence models for engineering applications, AIAA Journal, 32, 1598–1605, https://doi.org/10.2514/3.12149, 1994.

Montalà, R., Lehmkuhl, O., and Rodriguez, I.: On the effects of the spanwise length on the flow past an airfoil in stall at moderate Reynolds numbers, Physics of Fluids, 38, 045 137, https://doi.org/10.1063/5.0317006, 2026.

Neuhaus, L., Wächter, M., and Peinke, J.: The fractal turbulent–non-turbulent interface in the atmosphere, Wind Energy Science, 9, 439–452, https://doi.org/10.5194/wes-9-439-2024, 2024.

Park, J. S., Witherden, F. D., and Vincent, P. E.: High-Order Implicit Large-Eddy Simulations of Flow over a NACA0021 Aerofoil, AIAA Journal, 55, 2186–2197, https://doi.org/10.2514/1.J055304, 2017.

Ragni, D. and Ferreira, C.: Effect of 3D stall-cells on the pressure distribution of a laminar NACA64-418 wing, Experiments in Fluids, https://doi.org/10.1007/s00348-016-2215-8, 2016.

Visbal, M. R. and Benton, S. I.: Exploration of high-frequency control of dynamic stall using large-eddy simulations, AIAA Journal, https://doi.org/10.2514/1.J056720, 2018.

Winkelman, A. E. and Barlow, J. B.: Flowfield Model for a Rectangular Planform Wing beyond Stall, AIAA Journal, 18, 1006–1008, https://doi.org/10.2514/3.50846, 1980.

Yon, S. A. and Katz, J.: Study of the Unsteady Flow Features on a Stalled Wing, AIAA Journal, 36, 305–312, https://doi.org/10.2514/2.372, 1998.

Zahle, F., Barlas, A., Lønbæk, K., Bortolotti, P., Zalkind, D., Wang, L., Labuschagne, C., Sethuraman, L., and Barter, G.: Definition of the IEA Wind 22-Megawatt Offshore Reference Wind Turbine, Technical University of Denmark, https://doi.org/10.11581/DTU.00000317, dTU Wind Energy Report E-0243 IEA Wind TCP Task 55, 2024.